Fitting local repolarization parameters in cardiac reaction-diffusion models in the presence of electrotonic coupling

Akshay Kota Aswath Kumar, Angelina Drahi, Vincent Jacquemet[a,b]

[a] *Université de Montréal, Département de Physiologie Moléculaire et Intégrative, Institut de Génie Biomédical, Montréal, Canada*
[b] *Hôpital du Sacré-Coeur de Montréal, Centre de Recherche, Montréal, Canada*

Correspondence to:

Vincent Jacquemet
Hôpital du Sacré-Coeur de Montréal
Centre de Recherche
5400 boul. Gouin Ouest
Montreal (Quebec)
Canada H4J 1C5
phone: +1 514 338 2222 ext. 2522
fax: +1 514 338 2694
vincent.jacquemet@umontreal.ca

Published in:

Comput. Biol. Med. (2017), vol. 81, pp. 55-63

Abstract

Background: Repolarization gradients contribute to arrhythmogenicity. In reaction–diffusion models of cardiac tissue, heterogeneities in action potential duration (APD) can be created by locally modifying an intrinsic membrane kinetics parameter. Electrotonic coupling, however, acts as a confounding factor that modulates APD dispersion.

Method: We developed an algorithm based on a quasi-Newton method that iteratively adjusts the spatial distribution of a membrane parameter to reproduce a predefined target APD map in a coupled tissue. The method assumes that the relation between the adjustable parameter and APD is bijective in an isolated cell. Each iteration of the algorithm involved simulating the cardiac reaction–diffusion system with the

updated parameter profile for one beat and extracting the APD map. The algorithm was extended to simultaneous estimation of two parameter profiles based on two APD maps at different repolarization thresholds.

Results: The method was validated in 1D, 2D and 3D atrial tissues using synthetic target APD maps with controllable total variation and maximum APD gradient. The adjustable parameter was local acetylcholine concentration. The iterations converged provided that APD gradients were not too steep. Convergence was found to be faster (2 to 5 iterations) when the maximal gradient was less steep, when APD range was smaller and when tissue conductivity was reduced.

Conclusion: This algorithm provides a tool to automatically generate arrhythmogenic substrates with controllable repolarization gradients and possibly incorporate experimental APD maps into computer models.

Keywords: computer modeling; cardiac electrophysiology; parameter estimation; action potential duration; cell coupling

---

1. Introduction

The presence of strong repolarization gradients in a cardiac tissue is an arrhythmogenic factor that promotes wave breaks and reentry [1–4]. The occurrence of functional block has been observed in the presence of action potential duration (APD) gradients above a critical value of the order of 2 to 12.5 ms/mm [5–8]. Dispersion of action potential duration (APD) may result from intrinsic spatial variations in ion channel density (notably aggravated by the remodeling induced by successive episodes of arrhythmia), from beat-to-beat variability in repolarization eventually exhibiting non-linear dynamics and chaos [9], or from the interplay between geometry, conduction properties, wavelet dynamics [10, 11], and mechano-electric feedback [12, 13].

Electrotonic currents flowing through gap junctions tend to reduce the differences in APD between neighboring cells [14–16]. As a result, APD measurements in an intact tissue may not exactly reflect the intrinsic local properties of the cells, but rather an average over a surrounding region whose size and shape depends on conduction properties [17, 18]. Determination of true intrinsic membrane properties may be obtained through biopsies followed by patch clamp experiments. This approach is however limited in terms of spatial resolution, creates damage to the tissue and possibly changes the dynamics and densities of ionic currents, resulting in an APD that may differ from the APD that would have been measured in situ. Techniques such as electrical stimulation, monophasic action potentials and optical mapping preserve the integrity of the tissue (to some extent), but the resulting APD maps are affected by electrotonicity. Thus, the relationship between measured APD and intrinsic APD is relevant to the non-destructive extraction of cellular intrinsic properties.

In computer models of cardiac arrhythmia, the incorporation of APD dispersion requires designing a spatial profile of intrinsic properties of cardiac cells. Typically, a membrane kinetics parameter is chosen as target and its spatial distribution is used as an input to the model [19, 20]. The question arises whether that parameter distribution can be determined from an APD map in the coupled tissue. The existence and uniqueness of the solution has been investigated in a simplified model with exponentially-shaped action potentials [21]. Hurtado et al. calibrated a ventricular model to reproduce the relation between activation time and a refractoriness parameter [22]. Defauw et al. proposed a Gaussian Green's function model and a deconvolution approach to estimate the intrinsic APD map [17]. Inspired by their approach, we hypothesized that knowledge about which specific membrane kinetics parameter causes APD variations would enable the development of more accurate methods.

In this paper, we propose an algorithm for iteratively computing the parameter

distribution that reproduces a target APD map, based on an idea initially sketched in [21] and tested in [23]. The implementation is described and extensively validated in atrial tissue models with increasing complexity, and its computational performance and accuracy are evaluated.

2. Methods

2.1. Problem statement

In the framework of a monodomain model of cardiac tissue, let us consider that the membrane model depends on a local parameter k that lies within a physiological range $[k_{\min}, k_{\max}]$. This parameter could be an ion channel conductance, an ionic concentration, or a normalized parameter describing the transition between normal and diseased tissue, but is assumed not to affect intercellular coupling (gap junction conductances). After spatial discretization, tissue configuration is described by a vector $\mathbf{k}$ whose size is the number of nodes in the mesh.

When the spatial distribution of k is non-uniform, the simulated APD map is also non-uniform. The forward problem then consists in computing the APD map ($\mathbf{a}$) as a function of $\mathbf{k}$

$$\mathbf{a} = \mathbf{a}_{\text{forw}}(\mathbf{k}; G) \ . \tag{1}$$

Because of electrotonicity, APD distribution depends not only on $\mathbf{k}$ but also on the intercellular coupling matrix G. Practically, the function $\mathbf{a}_{\text{forw}}$ was evaluated by running a monodomain simulation with the distribution of parameters set to $\mathbf{k}$ and by measuring the APD map. Specific simulation methods are described in Sect. 2.5.

Assuming that the coupling is known, the inverse problem consists in recovering the parameter distribution $\mathbf{k}$ that would reproduce a given APD map $\mathbf{a}_{\text{target}}$

$$\mathbf{k} = \mathbf{a}_{\text{forw}}^{-1}(\mathbf{a}_{\text{target}}; G) \ , \tag{2}$$

provided that the solution exists and is unique for a given stimulation protocol, i.e. $\mathbf{a}_{\text{forw}}$ is invertible. Uniqueness of the solution has been proved in a simple analytical model [21] and is also guaranteed if the APD map in the coupled system can be written as the convolution of the intrinsic APD map with a spatial (e.g. Gaussian) filter [17].

2.2. Parameter identification

The inverse problem is equivalent to solving the equation $\mathbf{a}_{\text{forw}}(\mathbf{k}) - \mathbf{a}_{\text{target}} = 0$. Our approach relies on the fact that the problem is easily solved when cells are uncoupled ($G = 0$). A first approximation $\mathbf{k}^{(0)}$ is obtained by neglecting electrotonicity:

$$\mathbf{k}^{(0)} = \mathbf{a}_{\text{forw}}^{-1}(\mathbf{a}_{\text{target}}; 0) \ . \tag{3}$$

Then, at iteration n, the parameter profile is updated using the quasi-Newton formula

$$\mathbf{k}^{(n+1)} = \mathbf{k}^{(n)} - \left(\mathbf{D}\mathbf{a}_{\text{forw}}(\mathbf{k}^{(n)}; 0)\right)^{-1} \cdot \left(\mathbf{a}_{\text{forw}}(\mathbf{k}^{(n)}; G) - \mathbf{a}_{\text{target}}\right) \ , \tag{4}$$

where the Jacobian $\mathbf{D}\mathbf{a}_{\text{forw}}(\mathbf{k}^{(n)}; G)$ has been approximated by the (diagonal) Jacobian in the uncoupled tissue $\mathbf{D}\mathbf{a}_{\text{forw}}(\mathbf{k}^{(n)}; 0)$ to avoid expensive computations. The Jacobian in the coupled tissue is indeed a fully-populated matrix. The diagonal approximation, which is reminiscent of mass lumping in finite element methods, guarantees that the inverse exists. Moreover, if the simulated local APD is shorter than the target APD, the local parameter k will be updated to increase the intrinsic APD, therefore increasing the updated simulated APD provided that this effect is not compensated by the neighboring cells. This overcompensation will not occur as long as the APD error is a smooth function of space. The iteration process stops when the error $\|\mathbf{a}_{\text{forw}}(\mathbf{k}^{(n)}) - \mathbf{a}_{\text{target}}\|$ falls below a tolerance, typically 1 ms.

2.3. Computational issues

As a preprocessing step, the relation $a = \alpha(k)$ between the parameter k and the APD (a) was studied in an isolated cell. The function α was evaluated (using simulations)

at $n = 8$ equally-spaced points in the interval $[k_{\min}, k_{\max}]$. The number of points was then iteratively increased until the maximal error between spline interpolation based on the previous iteration and the new computed data points fell below a threshold, typically 0.5 ms. This provided a piece-wise polynomial interpolation for the function $\alpha(k)$. The monotonicity of $\alpha(k)$ was checked using the coefficient of the polynomials. Spline interpolation on the same data points (reflected across the diagonal) was used to compute the inverse function $k = \alpha^{-1}(a)$. The derivative $\alpha'(k)$ was obtained by analytically differentiating the piece-wise polynomial in each of its segments. To avoid out-of-bound errors, when the argument of the function is out of the domain or the range of α, the value at the bound is returned.

With these notations, we have:

$$\mathbf{a}^{-1}_{\text{forw}}(\mathbf{a}_{\text{target}}; 0) = \alpha^{-1}(\mathbf{a}_{\text{target}}) \tag{5}$$

$$(\mathbf{D}\mathbf{a}_{\text{forw}}(\mathbf{k}; 0))^{-1} = \text{diag}(\alpha'(\mathbf{k}))^{-1} , \tag{6}$$

where the functions α^{-1} and α' are applied element-wise and 'diag' creates a diagonal matrix from a diagonal vector.

The algorithm was implemented in Matlab on a Linux machine. At each iteration, the Matlab function writes a parameter file, calls an external program to run the simulation, reads the output and continues the execution in Matlab.

2.4. Extension to two parameters

If the membrane model depends on two parameters k and m, two measures of repolarization $a = \alpha(k, m)$ and $b = \beta(k, m)$ are needed for parameter identification. They may represent APD at different repolarization thresholds or at different heart rates. Assuming that the system $a = \alpha(k, m)$ and $b = \beta(k, m)$ has a unique solution in a domain Ω, the inverse solution may be denoted by $k = \alpha^{-1}(a, b)$ and $m = \beta^{-1}(a, b)$.

In a coupled tissue where the two measures $\mathbf{a}_{\text{forw}}(\mathbf{k},\mathbf{m})$ and $\mathbf{b}_{\text{forw}}(\mathbf{k},\mathbf{m})$ can be simulated, a first estimate of the parameter vectors $\mathbf{k}$ and $\mathbf{m}$ that solve the inverse problem $\mathbf{a}_{\text{target}} = \mathbf{a}_{\text{forw}}(\mathbf{k},\mathbf{m})$ and $\mathbf{b}_{\text{target}} = \mathbf{b}_{\text{forw}}(\mathbf{k},\mathbf{m})$ is obtained by

$$\mathbf{k}^{(0)} = \alpha^{-1}(\mathbf{a}_{\text{target}}, \mathbf{b}_{\text{target}}) \tag{7}$$

$$\mathbf{m}^{(0)} = \beta^{-1}(\mathbf{a}_{\text{target}}, \mathbf{b}_{\text{target}}) \ . \tag{8}$$

Then, at iteration n the update formula reads

$$\begin{pmatrix} \mathbf{k}^{(n+1)} \\ \mathbf{m}^{(n+1)} \end{pmatrix} = \begin{pmatrix} \mathbf{k}^{(n)} \\ \mathbf{m}^{(n)} \end{pmatrix} - J(\mathbf{k}^{(n)}, \mathbf{m}^{(n)})^{-1} \cdot \begin{pmatrix} \mathbf{a}_{\text{forw}}(\mathbf{k}^{(n)}, \mathbf{m}^{(n)}) - \mathbf{a}_{\text{target}} \\ \mathbf{b}_{\text{forw}}(\mathbf{k}^{(n)}, \mathbf{m}^{(n)}) - \mathbf{b}_{\text{target}} \end{pmatrix} \tag{9}$$

where the Jacobian is approximated by

$$J(\mathbf{k},\mathbf{m}) = \begin{pmatrix} \text{diag}((\partial_k \alpha)(\mathbf{k},\mathbf{m})) & \text{diag}((\partial_m \alpha)(\mathbf{k},\mathbf{m})) \\ \text{diag}((\partial_k \beta)(\mathbf{k},\mathbf{m})) & \text{diag}((\partial_m \beta)(\mathbf{k},\mathbf{m})) \end{pmatrix} \tag{10}$$

where the functions $\partial_k \alpha$, etc. are applied element-wise. The inverse of J is easily computed thanks to its 2-by-2 diagonal block structure:

$$J^{-1} = \begin{pmatrix} D_{11} & D_{12} \\ D_{21} & D_{22} \end{pmatrix}^{-1} = \begin{pmatrix} \Delta^{-1} D_{22} & -\Delta^{-1} D_{21} \\ -\Delta^{-1} D_{12} & \Delta^{-1} D_{11} \end{pmatrix} \tag{11}$$

where $\Delta = D_{11}D_{22} - D_{12}D_{21}$ and all the D matrices are diagonal.

The implementation is similar to the one-parameter case. The functions α and β are approximated using cubic interpolation on a 2D grid (Matlab function `interp2`). The partial derivatives are computed numerically with finite differences. The inverse functions are also computed by interpolation (`TriScatteredInterp`).

2.5. Simulation methods

Practically, the algorithm requires as input the specification of the adjustable parameter k, the interval $[k_{\min}, k_{\max}]$, the single-cell function $\alpha(k)$ and the forward simulator

$\mathbf{a}_{\text{forw}}(\mathbf{k})$. This includes the specification of a tissue model and stimulation protocol as well as the definition of APD.

Unless otherwise stated (notably Sect. 3.5), the Ramirez et al. membrane model [24] was used. This non-linear model of canine atrial myocyte takes into account 14 ionic currents including an acetylcholine-dependent K^+ current ($I_{K(ACh)}$) [19], variations of intracellular concentrations (Na^+, K^+, Ca^{2+}) and calcium dynamics in the sarcoplasmic reticulum, for a total of 26 ordinary differential equations. The non-dimensional parameter k was defined as a function of acetylcholine concentration (ACh) in μM:

$$k = \frac{10}{1 + 9.13652 \cdot \text{ACh}^{-0.477811}} \ . \tag{12}$$

This expression is the first factor in the formulation of the $I_{K(ACh)}$ current. The interval $[k_{\min}, k_{\max}] = [0, 0.1]$ corresponds approximately to the ACh range considered in Kneller et al. [19].

APD was measured at a -70 mV threshold, which is near 90% repolarization in this model. The resulting functions $\alpha(k)$ and $\alpha'(k)$ and their validation are represented in Fig. 1.

The function $\mathbf{a}_{\text{forw}}(\mathbf{k})$ was computed by running a monodomain simulation in 1D (5-cm long cable), 2D (5-by-2.5 cm sheet of tissue) or 3D (atrial model [27]) in finite difference regular grids. The vector $\mathbf{k}$ encoded ACh concentration at every node of the grid. The entire tissue was stimulated simultaneously with an intracellular current of 50 μA/cm^2, which approximately corresponds to 1.5$\times$ threshold, applied after 50 ms at rest to let the tissue reach steady state. When all cells were back to resting state, the simulation stopped and the APD map was outputted.

3. Results

3.1. Convergence of the iterations

Convergence of the algorithm was tested in a one-dimensional cable model. The tissue was a 5-cm long cable consisting of 250 nodes ($\Delta x = 200$ μm) with Ramirez et al. membrane kinetics [24]. The conductivity was $\sigma = 0.5$, 1 or 2 mS/cm. The target APD profile was a sigmoid curve (hyperbolic tangent) characterized by a mean value of 120 ms, an amplitude of APD variation (max - min) of 0 to 60 ms and a maximal gradient from 0 to 30 ms/mm.

Figure 2 shows examples of inverse solutions obtained by adjusting the local concentration of ACh. The initial iteration provided a reasonable estimate (white circles) although the APD gradient was significantly underestimated due to the filtering effect of electrotonicity. The errors on the maximum gradient after the initial step were 17%, 35% and 48% in panels A, C and E respectively. After 2-10 iterations, convergence was reached (maximal error < 1 ms). When the target APD gradient was steeper than the gradient that would be generated by a discontinuity (step function) in ACh concentration, the ACh profile obtained was not monotonic (Figs. 2D,F). At some point, ACh concentration would need to "become negative" to further steepen the gradient so the inverse problem had no solution.

The number of iterations needed to decrease the maximal error in APD below 1 ms is presented in Fig. 3. More iterations were required when the target APD gradient was steeper, when the tissue conductivity was higher, and when the APD range was smaller (for a given APD gradient). To reproduce steep gradients, over 10 iterations may be needed. However, physiological solutions in which the ACh profile was monotonic (as in Fig. 2B) only required ≤ 3 iterations (small dots in Fig. 3).

Using all conditions for which the solution existed and the iterations converged ($n =$

507 target APD maps, from Fig. 3), the rate of convergence was estimated by displaying the maximal error along the iterations (Fig. 4). The rate of convergence was slower than that of the original Newton method because the Jacobian was only approximated and off-diagonal elements were neglected. The error was nevertheless divided by 10 after 5–6 iterations. Attempting to decrease the maximum error below 0.1 ms is debatable since APD computation was based on linear interpolation of membrane potentials stored every 0.1 ms.

3.2. Accuracy of the inverse solver

To assess the accuracy of the algorithm, a sinusoidal ACh profile similar to the configuration of Kneller et al. [19] was set up in the same cable as the previous section (5 cm long, $\sigma = 1$ mS/cm). The spatial variation of ACh (in nM) was formulated as $\mathrm{ACh}(x) = 0.6 + 0.4\cos(2\pi x/\lambda)$, where the wavelength λ, representing the distance between two consecutive local maxima of the target sinusoidal ACh profile, ranged from 0.2 to 10 cm.

The APD profile corresponding to each of these configurations was computed and the ACh profile obtained by solving the inverse problem was compared at each iteration to the target ACh profile. The relative error was defined as the maximal difference between the target ACh profile and the inverse solution, divided by ACh range (0.8 nM).

The resulting APD profile was approximately sinusoidal. At short wavelength, however, the amplitude of the variations in APD was reduced due to the smoothing effect of electrotonicity. The steepest APD gradient was maximal for a wavelength of 1.25 cm (Fig. 5A).

The relative error decreased with the iterations (Fig.. 5B), but was systematically larger for shorter wavelengths, i.e. for steep spatial variations in ACh. The iterations converged to the target ACh profile for all wavelength values, suggesting that the so-

lution to the inverse problem is unique. However, while 10 iterations were sufficient to achieve a relative error $< 1\%$ at a wavelength of 1.25 cm, 378 iterations were needed when the wavelength was 0.2 cm. This demonstrates how electrotonic effects filter out high-frequency information in agreement with their approximate representation as convolution operators (e.g. Gaussian) acting on the intrinsic APD map [17, 21, 25].

3.3. Anisotropy

The effect of anisotropy on the convergence of the inverse solver was assessed in a two-dimensional tissue (5×2.5 cm, $\Delta x = \Delta y = 200$ μm) with Ramirez et al. membrane kinetics. Three sets of conductivity values were used: (1) 1 mS/cm (isotropic), (2) 1.25 mS/cm (longitudinal) and 0.67 mS/cm (transverse), and (3) 2 mS/cm (longitudinal) and 0.5 mS/cm (transverse), thereby incrementally increasing the anisotropy ratio while keeping the product of longitudinal and transverse conductivities constant.

The target APD profile was a sigmoid function (hyperbolic tangent) of the distance to the bottom-left corner and ranged from 105 to 135 ms, as illustrated in Fig. 6A. The maximal gradient was varied from 0 to 20 ms/mm. The computed ACh map corresponding to the target APD map of panel A is displayed in panel B.

Figure 6C shows the number of iterations needed to reach 1 ms accuracy. In the isotropic case, convergence was similar to the one-dimensional case (Fig. 3). As the anisotropy ratio increased, more iterations were needed for convergence. Non-monotonicity occurred at gradients ≥ 5 ms/mm (also similar to the one-dimensional case), as in in Fig. 6B.

3.4. 3D geometry

Extension to more realistic conditions was tested in a simple model of the atria with rule-based fiber orientation [26, 27] (Fig. 7A). To enable comparison with 1D and 2D

results, the Ramirez et al. model was used and the whole tissue was simultaneously stimulated to simulate APD maps. The longitudinal/transverse conductivities were set to 2/0.5 mS/cm, 4/1 mS/cm or 9/3 mS/cm, the latter configuration representing the baseline values in [27].

Generation of target APD maps was based on random distributions of patches [23, 28]. Four realizations were generated; one is shown on Fig. 7A. This defined a map $u_0(\mathbf{x})$ such that $u_0 = 0$ inside the colored patches and $u_0 = 1$ outside. In order to control the gradient, a Gaussian spatial filter was applied by solving an isotropic diffusion equation $\partial u/\partial t = \Delta u$ with $u(\mathbf{x}, 0) = u_0(\mathbf{x})$ and no-flux boundary condition. The simulation code designed for the monodomain equation was used to solve the diffusion equation on the same grid. Analytical calculations in 1D suggest that the solution at time $T = \lambda^2/2$ provides a map in the range $[0, 1]$ with maximum gradient of approximately $(\sqrt{2\pi}\lambda)^{-1}$. Accordingly, the target APD map was set to $a(\mathbf{x}) = a_0 + \Delta a \cdot u(\mathbf{x}, T)$, where $a_0 = 105$ ms, $\Delta a = 30$ ms and $T = \Delta a^2/(4\pi\gamma^2)$. The gradient parameter γ was either 2, 3.5 or 5 ms/mm. Combined with the four realizations, this gave 12 target APD maps (e.g. Fig. 7B) whose gradients were validated using numerical finite differences to check consistency.

The inverse problem was solved for the 12 target APD maps and the 3 conduction properties, and the resulting ACh profiles were determined. An example is shown in Fig. 7C. Convergence was assessed by computing the 99th percentile of the absolute value of the difference between the simulated and the target APD maps. In some grid points (notably at the boundary of the tissue or at the junction with the conducting system), the absolute error may not decrease below a few milliseconds so the percentile was used as an error metric instead of the maximum in order to avoid overfitting.

The convergence results (Fig. 8) confirm that more iterations are needed when the gradient is steeper and when the conductivities are higher. In the extreme case (white

circles in panel C), no solution existed and the iterations converged towards an ACh profile with zero values near the steepest gradients, similarly to the results in a cable (Fig. 2D). Nevertheless, for slow APD variations (2 ms/mm as in Fig. 7B), 4 iterations were sufficient to reduce the 99th-percentile error below 1 mm.

3.5. Estimation of two parameters

The algorithm for simultaneously estimating two parameters was tested in a one-dimensional tissue. The Courtemanche et al. [29] membrane kinetics model was used in order to simulate a wider range of action potential morphology. Two parameters were varied: a multiplication factor for the L-type calcium current (P_{CaL} in the range $[0.5, 1]$; 0.8 means 20% inhibition) and one for the transient outward current (P_{to} in the range $[0, 1]$). APDs were measured both at -70 and -30 mV, thus providing the two required measures a and b from subsection 2.4. The relation between the two parameters and the two repolarization measures, illustrated in Fig. 9, is a one-to-one mapping that defines the functions α^{-1} and β^{-1}.

For the sake of illustration, we created a gradient in $\mathrm{APD}_{-30\,\mathrm{mV}}$ (hyperbolic tangent from 120 to 160 ms with a maximal gradient of 3 ms/mm) and constant $\mathrm{APD}_{-70\,\mathrm{mV}} =$ 270 ms in the same cable as previous simulations (5 cm, 250 elements, 2 mS/cm conductivity). The two-parameter inverse solver was applied to identify the profiles of P_{CaL} and P_{to}. The initial estimate had error up to a 2.6 ms. After two iterations, the maximum error was below 1 ms for both target APD maps. The converged solution is displayed on Fig. 10. The bottom panel shows how both parameters have to adjust to increase $\mathrm{APD}_{-30\,\mathrm{mV}}$ while keeping $\mathrm{APD}_{-70\,\mathrm{mV}}$ constant. The shapes of the resulting action potentials are shown in Fig. 9B.

4. Discussion

We developed an algorithm for estimating membrane kinetics parameters from an APD map in the presence of electrotonic coupling. As compared to Defauw et al. [17] whose Gaussian deconvolution technique enabled estimation of the intrinsic APD from the measured APD, we achieved better accuracy at the expense of further assumptions on the cause of APD variations (the membrane parameter responsible for APD gradients has to be known) and more computational time. Note that Defauw et al. [17] also required knowledge about conductivity and anisotropy. Our approach is therefore more appropriate in the context of modeling, where we aim at incorporating experimental data into the model and controlling parameters such as APD gradients in order to better design numerical experiments.

The initial estimate based on neglecting coupling underestimated APD gradients but was a reasonable approximation of the solution (usually at most 2-5 ms error, sometimes up to 10 ms, or about 5-10% relative error). As a result, the subsequent Newton iterations always converged provided that the solution existed. Non-existence of the solution occurred when the APD gradient was too strong for a given conductivity, in agreement with a simple theoretical model [21]. Very strong APD gradients were only observed in the presence of poor coupling. The closer the APD gradient to the critical gradient, the more iterations were needed for convergence. Inverse solutions with non-monotonic variations in ACh were computed to demonstrate the performance of the algorithm in extreme cases where hand-made fine-tuning would be difficult. In more physiological conditions, however, a few iterations were sufficient to reach 1-ms accuracy. This corresponds to $< 1\%$ relative error since the APDs were always > 100 ms.

The performance of the algorithm was globally preserved when increasingly com-

plex models were used, from 1D to 3D with anisotropy. The approach would remain applicable to more realistic cardiac models. Notably, bidomain models can improve the description of the spatial distribution of repolarization [30, 31]. Also, while this paper focused on atrial models, the much thicker ventricular wall offers opportunities for future applications because of the importance of repolarization gradients in the genesis of the T wave [32]. Improvements of the mathematical description of current diffusion in a cardiac tissue based on fractional diffusion and porous-medium approaches have recently been proposed [18, 33, 34]. Our parameter estimation approach would also apply in these cases.

In the presence of conduction heterogeneity, local fluctuations in electrotonic load can affect the APD. When a smooth target APD map is selected, there is a risk of trying to overfit those small local fluctuations. A regularization approach may be applicable to identify the best smooth solution. Note that since our inverse problem has a unique solution (if any, and if the single cell problem has a unique solution), regularization is not strictly required. Here, we simply defined the error metric as the 99th percentile of absolute error to avoid this problem.

In the presence of noise on the target APD map, two options are possible. One would be to use regularization. The consequence would be to limit the maximum gradient of the parameter profile, although even a smooth APD map may be the result of a discontinuous parameter profile. Another approach would be to numerically determine the maximum APD gradient that can be reproduced in the model, and then filter the experimental APD map such that the APD gradients are everywhere smaller than the critical gradient.

If the APD map is only known at a limited number of locations as often experimentally, interpolation is necessary. A priori information about the spatial variations of APD (e.g. smoothness) must be assumed. Laplacian or radial basis function inter-

polation can be used to specify the target APD at every node of the mesh, and then the algorithm can be run as previously.

The method easily extends to the estimation of two or more parameters. In the limited set of scenarios that we tested, the number of iterations needed were not significantly larger. An issue though is the requirement of a one-to-one relation between parameters and APD measures. In many situations, the solution to the inverse problem in a single cell may not be unique and a subset of the parameter space must be chosen, which could be challenging in three or more dimensions. A possible application of two-parameter estimation is to simultaneously reproduce APD at different cycle lengths. This constitutes a first step toward fitting spatially-varying APD restitution curves [35] and is relevant to the design of substrates for conduction blocks and reentry [5, 36]. A more complex application would be to reproduce the odd-beat and even-beat APD maps during discordant alternans [37] at a given pacing rate by fitting two parameters. Dependence on pacing site and stimulation history [38] would however make it challenging to completely reproduce the spatio-temporal alternans patterns. The rationale for choosing the Ramirez et al. model with ACh variations was precisely that it has low rate-adaptation and parameters can be estimated based on a single beat. The same approach is however expected be applicable to other model formulations and types of parameters.

APD slightly depends on activation pattern and propagation direction and is affected by collision between wave fronts and with boundaries [10, 16, 17]. We deliberately avoided that confounding factor by stimulating the whole tissue simultaneously. Our approach still applies when APD is computed during normal sinus rhythm propagation, with similar performance in terms of accuracy and convergence, as suggested by our recent preliminary results in a 3D atrial model extending this paper [23], provided that boundary and collision effects are accounted for in the target APD map.

Despite its relevance to arrhythmogenicity [1, 39, 40], accurate measurement of APD gradients in animal models or in patients remains challenging. Repolarization is more difficult to map than depolarization and gradients may be underestimated due to low spatial resolution or spatial filtering. Emerging technology may improve the reliability of measurements [41]. Meanwhile, computer modeling provides a way to accurately control the steepness of APD gradients and assess their effect on arrhythmogenicity [42–45]. The tools presented in this paper facilitate the design of these simulation studies.

Conflict of interest statement

None declared.

Acknowledgments

This work was supported by the Natural Sciences and Engineering Research Council of Canada (NSERC grant RGPIN-2015-05658) and by the Mitacs Globalink program.

References

[1] S. Fareh, C. Villemaire, S. Nattel, Importance of refractoriness heterogeneity in the enhanced vulnerability to atrial fibrillation induction caused by tachycardia-induced atrial electrical remodeling, Circulation 98 (20) (1998) 2202–9.

[2] J. Zhou, B. J. Scherlag, J. Edwards, W. M. Jackman, R. Lazzara, S. S. Po, Gradients of atrial refractoriness and inducibility of atrial fibrillation due to stimulation of ganglionated plexi, J Cardiovasc Electrophysiol 18 (1) (2007) 83–90.

[3] A. Bueno-Orovio, B. M. Hanson, J. S. Gill, P. Taggart, B. Rodriguez, In vivo human left-to-right ventricular differences in rate adaptation transiently increase pro-arrhythmic risk following rate acceleration, PLoS One 7 (12) (2012) e52234.

[4] T. Opthof, M. J. Janse, V. M. Meijborg, J. Cinca, M. R. Rosen, R. Coronel, Dispersion in ventricular repolarization in the human, canine and porcine heart, Prog Biophys Mol Biol 120 (1) (2016) 222–235.

[5] K. J. Sampson, C. S. Henriquez, Simulation and prediction of functional block in the presence of structural and ionic heterogeneity, Am J Physiol Heart Circ Physiol 281 (6) (2001) H2597–603.

[6] W. B. Gough, R. Mehra, M. Restivo, R. H. Zeiler, N. El-Sherif, Reentrant ventricular arrhythmias in the late myocardial infarction period in the dog. 13. Correlation of activation and refractory maps, Circ Res 57 (3) (1985) 432–442.

[7] T. Osaka, I. Kodama, N. Tsuboi, J. Toyama, K. Yamada, Effects of activation sequence and anisotropic cellular geometry on the repolarization phase of action potential of dog ventricular muscles, Circulation 76 (1) (1987) 226–236.

[8] M. Restivo, W. Gough, N. el Sherif, Ventricular arrhythmias in the subacute myocardial infarction period. High-resolution activation and refractory patterns of reentrant rhythms, Circ Res 66 (5) (1990) 1310–1327.

[9] L. Glass, A. Goldberger, M. Courtemanche, A. Shrier, Nonlinear dynamics, chaos and complex cardiac arrhythmias, in: Proc R Soc Lond A, Vol. 413, 1987, pp. 9–26.

[10] E. M. Cherry, F. H. Fenton, Effects of boundaries and geometry on the spatial distribution of action potential duration in cardiac tissue, J Theor Biol 285 (1) (2011) 164–176.

[11] P. Comtois, A. Vinet, Curvature effects on activation speed and repolarization in an ionic model of cardiac myocytes, Phys Rev E 60 (4 Pt B) (1999) 4619–28.

[12] P. Taggart, M. Lab, Cardiac mechano-electric feedback and electrical restitution in humans, Prog Biophys Mol Biol 97 (2-3) (2008) 452–60.

[13] P. Colli Franzone, L. F. Pavarino, S. Scacchi, Joint influence of transmural heterogeneities and wall deformation on cardiac bioelectrical activity: A simulation study, Math Biosci 280 (2016) 71–86.

[14] M. D. Lesh, M. Pring, J. F. Spear, Cellular uncoupling can unmask dispersion of action potential duration in ventricular myocardium. A computer modeling study., Circ Res 65 (5) (1989) 1426–1440.

[15] R. Joyner, Modulation of repolarization by electrotonic interactions., Jap Heart J 27 (1986) 167–183.

[16] K. J. Sampson, C. S. Henriquez, Electrotonic influences on action potential duration dispersion in small hearts: a simulation study, Am J Physiol Heart Circ Physiol 289 (1) (2005) H350–H360.

[17] A. Defauw, I. V. Kazbanov, H. Dierckx, P. Dawyndt, A. V. Panfilov, Action potential duration heterogeneity of cardiac tissue can be evaluated from cell properties using Gaussian Green's function approach, PLoS ONE 8 (11) (2013) e79607.

[18] A. Bueno-Orovio, D. Kay, V. Grau, B. Rodriguez, K. Burrage, Fractional diffusion models of cardiac electrical propagation: role of structural heterogeneity in dispersion of repolarization, J R Soc Interface 11 (97) (2014) 20140352.

[19] J. Kneller, R. Zou, E. J. Vigmond, Z. Wang, L. J. Leon, S. Nattel, Cholinergic atrial fibrillation in a computer model of a two-dimensional sheet of canine atrial cells with realistic ionic properties, Circ Res 90 (9) (2002) e73–e87.

[20] R. H. Clayton, A. V. Holden, Dispersion of cardiac action potential duration and the initiation of re-entry: a computational study, Biomed Eng Online 4 (2005) 11.

[21] V. Jacquemet, A simple analytical model of action potential duration profile in electrotonically-coupled cells, Math Biosci 272 (2016) 92–9.

[22] D. E. Hurtado, E. Kuhl, Computational modelling of electrocardiograms: repolarisation and t-wave polarity in the human heart, Comput Methods Biomech Biomed Engin 17 (9) (2014) 986–96.

[23] A. Drahi, A. K. Aswath Kumar, V. Jacquemet, An algorithm for fitting local membrane parameters to an action potential duration map in a tissue with electrotonic interactions, in: Computing in Cardiology, 2016.

[24] R. J. Ramirez, S. Nattel, M. Courtemanche, Mathematical analysis of canine atrial action potentials: rate, reg ional factors, and electrical remodeling, Am J Physiol Heart Circ Physiol 279 (4) (2000) H1767–85.

[25] P. Comtois, A. Vinet, Stability and bifurcation in an integral-delay model of cardiac reentry including spatial coupling in repolarization, Phys Rev E 68 (5) (2003) 051903.

[26] M. W. Krueger, V. Schmidt, C. Tobón, F. M. Weber, C. Lorenz, D. U. Keller, H. Barschdorf, M. Burdumy, P. Neher, G. Plank, et al., Modeling atrial fiber orientation in patient-specific geometries: a semi-automatic rule-based approach, in: Functional imaging and modeling of the heart, Springer, 2011, pp. 223–232.

[27] V. Jacquemet, Modeling left and right atrial contributions to the ECG: A dipole-current source approach, Comput Biol Med 65 (2015) 192–9.

[28] V. Jacquemet, N. Virag, Z. Ihara, L. Dang, O. Blanc, S. Zozor, J.-M. Vesin, L. Kappenberger, C. Henriquez, Study of unipolar electrogram morphology in a computer model of atrial fibrillation, J Cardiovasc Electrophysiol 14 (10 Suppl) (2003) S172–9.

[29] M. Courtemanche, R. J. Ramirez, S. Nattel, Ionic mechanisms underlying human atrial action potential properties: insights from a mathematical model, Am J Physiol Heart Circ Physiol 275 (1) (1998) H301–H321.

[30] P. Colli Franzone, L. F. Pavarino, B. Taccardi, Simulating patterns of excitation, repolarization and action potential duration with cardiac bidomain and monodomain models, Math Biosci 197 (1) (2005) 35–66.

[31] I. R. Efimov, F. Aguel, Y. Cheng, B. Wollenzier, N. Trayanova, Virtual electrode polarization in the far field: implications for external defibrillation, Am J Physiol Heart Circ Physiol 279 (3) (2000) H1055–70.

[32] K. Gima, Y. Rudy, Ionic current basis of electrocardiographic waveforms: a model study, Circ Res 90 (8) (2002) 889–96.

[33] P. E. Hand, C. S. Peskin, Homogenization of an electrophysiological model for a strand of cardiac myocytes with gap-junctional and electric-field coupling, Bull Math Biol 72 (6) (2010) 1408–24.

[34] D. Hurtado, S. Castro, A. Gizzi, Computational modeling of non-linear diffusion in cardiac electrophysiology: A novel porous-medium approach, Comput Meth Appl Mech Eng 300 (2016) 70–83.

[35] J. N. Weiss, Z. Qu, P.-S. Chen, S.-F. Lin, H. S. Karagueuzian, H. Hayashi,

A. Garfinkel, A. Karma, The dynamics of cardiac fibrillation, Circulation 112 (8) (2005) 1232–40.

[36] J. J. Fox, M. L. Riccio, F. Hua, E. Bodenschatz, R. F. J. Gilmour, Spatiotemporal transition to conduction block in canine ventricle, Circ Res 90 (3) (2002) 289–96.

[37] J. M. Pastore, S. D. Girouard, K. R. Laurita, F. G. Akar, D. S. Rosenbaum, Mechanism linking T-wave alternans to the genesis of cardiac fibrillation, Circulation 99 (10) (1999) 1385–94.

[38] A. Gizzi, E. M. Cherry, R. F. J. Gilmour, S. Luther, S. Filippi, F. H. Fenton, Effects of pacing site and stimulation history on alternans dynamics and the development of complex spatiotemporal patterns in cardiac tissue, Front Physiol 4 (2013) 71.

[39] P. Sanders, O. Berenfeld, M. Hocini, P. Jaïs, R. Vaidyanathan, L.-F. Hsu, S. Garrigue, Y. Takahashi, M. Rotter, F. Sacher, et al., Spectral analysis identifies sites of high-frequency activity maintaining atrial fibrillation in humans, Circulation 112 (6) (2005) 789–797.

[40] M. F. Swartz, G. W. Fink, C. J. Lutz, S. M. Taffet, O. Berenfeld, K. L. Vikstrom, K. Kasprowicz, L. Bhatta, F. Puskas, J. Kalifa, et al., Left versus right atrial difference in dominant frequency, K+ channel transcripts, and fibrosis in patients developing atrial fibrillation after cardiac surgery, Heart Rhythm 6 (10) (2009) 1415–1422.

[41] T. Y. Yu, F. Syeda, A. P. Holmes, B. Osborne, H. Dehghani, K. L. Brain, P. Kirchhof, L. Fabritz, An automated system using spatial oversampling for optical mapping in murine atria. development and validation with monophasic and transmembrane action potentials, Prog Biophys Mol Biol 115 (2-3) (2014) 340–8.

[42] E. J. Vigmond, V. Tsoi, S. Kuo, H. Arevalo, J. Kneller, S. Nattel, N. Trayanova, The effect of vagally induced dispersion of action potential duration on atrial arrhythmogenesis, Heart Rhythm 1 (3) (2004) 334–44.

[43] M.-E. Ridler, M. Lee, D. McQueen, C. Peskin, E. Vigmond, Arrhythmogenic consequences of action potential duration gradients in the atria, Can J Cardiol 27 (1) (2011) 112–9.

[44] M. W. Krueger, A. Dorn, D. U. J. Keller, F. Holmqvist, J. Carlson, P. G. Platonov, K. S. Rhode, R. Razavi, G. Seemann, O. Dossel, In-silico modeling of atrial repolarization in normal and atrial fibrillation remodeled state, Med Biol Eng Comput 51 (10) (2013) 1105–19.

[45] E. Matene, A. Vinet, V. Jacquemet, Dynamics of atrial arrhythmias modulated by time-dependent acetylcholine concentration: a simulation study, Europace 16 Suppl 4 (2014) iv11–iv20.

Figures

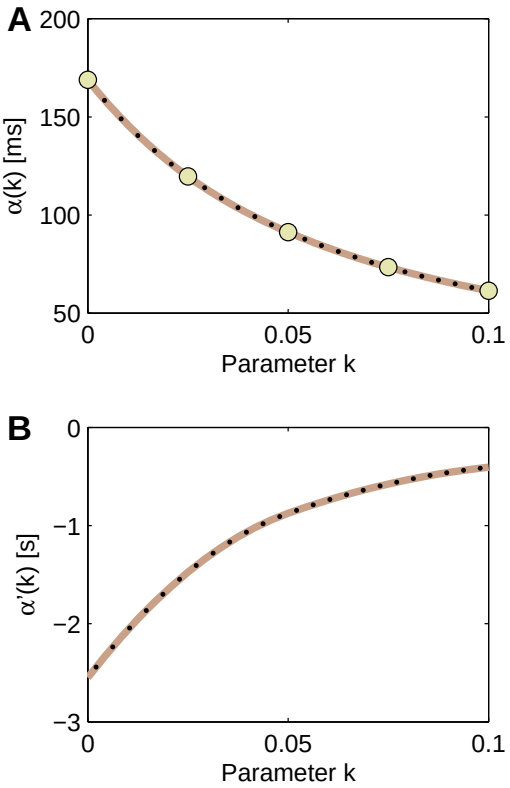

Figure 1: Action potential duration (α) as a function of the parameter k in a single cell using the Ramirez et al. model. (A) Function $\alpha(k)$: control points ($n = 5$ circles) from which spline interpolation was constructed (thick brown line); validation with single cell simulations (black dots); the error criterion corresponds to the maximal absolute difference between the thick line and the small dots. (B) Derivative $\alpha'(k)$: symbolic derivative of the spline interpolation function shown in panel A (thick brown curve); validation using numerical derivative based on single cell simulations (black dots).

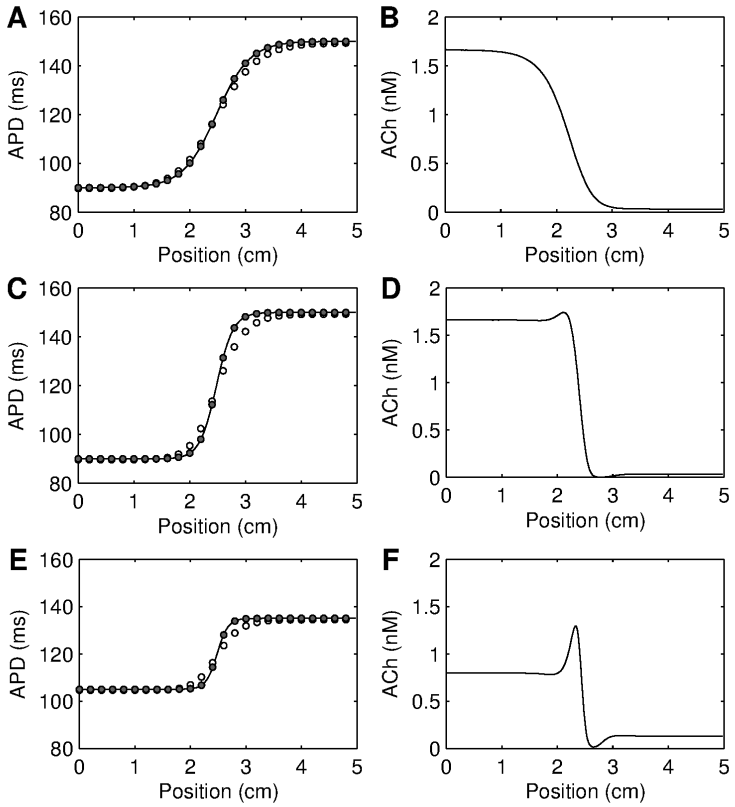

Figure 2: Inverse problem in a 1D cable (σ = 2 mS/cm). Action potential duration (APD) profile along a cable (left panels: A, C, E) showing the target APD profile (solid line), the first iteration (white circles) and the profile after convergence (gray circles). The target maximum APD gradient is: (A) 5 ms/mm, (C) 10 ms/mm, and (E) 7 ms/mm. The corresponding right panels (B, D, F) display the ACh profile after convergence.

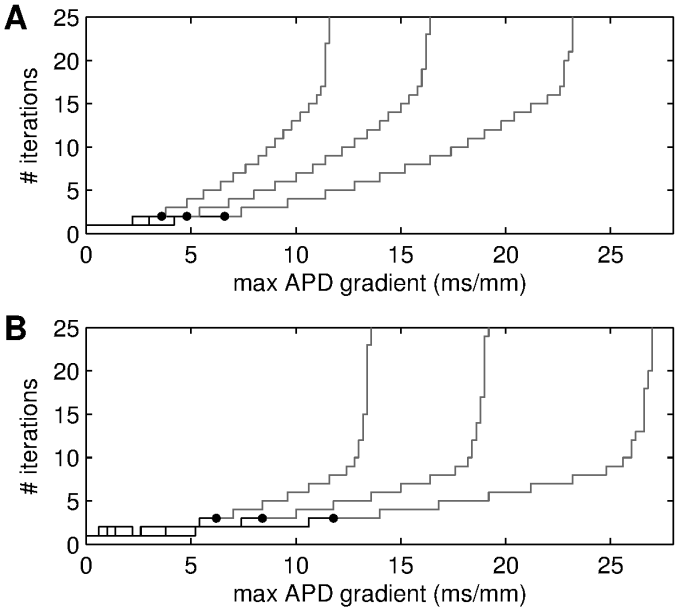

Figure 3: Number of iterations needed to solve the inverse problem in 1D with an error < 1 ms as a function of the maximal action potential duration (APD) gradient. The target APD profile was a sigmoid function as in Fig. 2 and ranged from 105 to 135 ms (A) or 90 to 150 ms (B). The conductivity of the tissue was 2, 1 and 0.5 mS/cm (curves from left to right on each panel). The dots denote the critical gradient above which the resulting ACh profile was not monotonic (gray part of the curves).

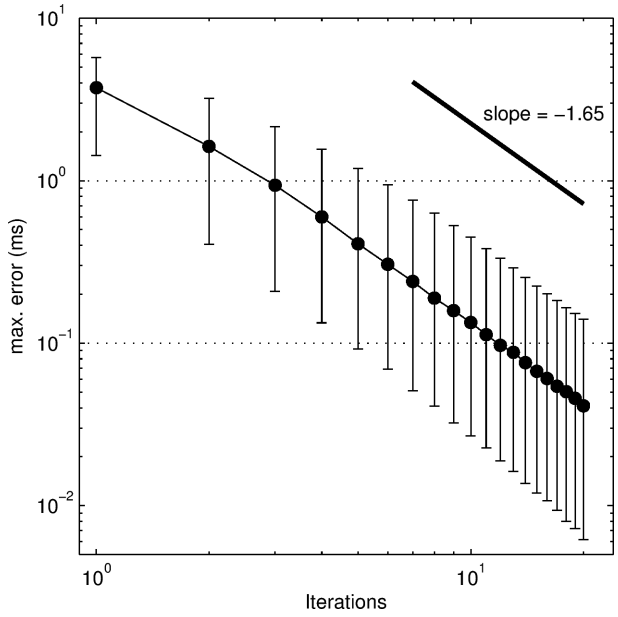

Figure 4: Maximal error as a function of the iterations in the 1D simulations of Fig. 3 that converged (averaged over $n = 507$ target APD maps). The error bars show the median and quartiles. The straight line with a slope of -1.65 illustrates the rate of convergence.

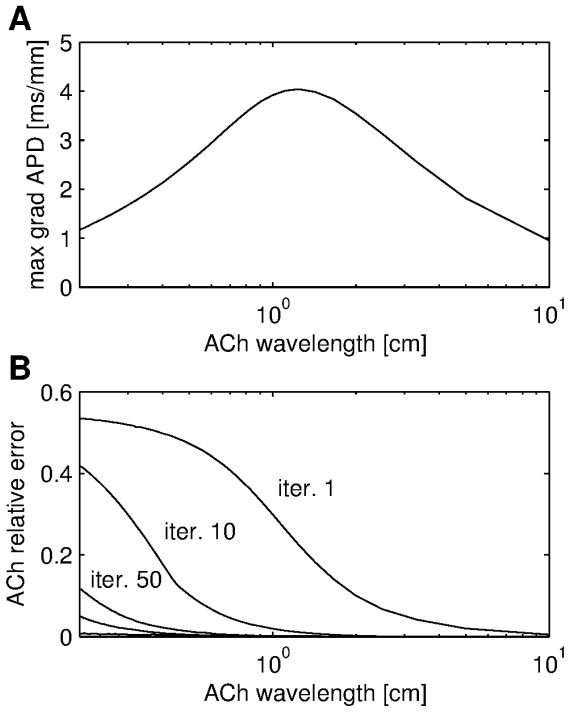

Figure 5: Accuracy of the inverse problem in a 1D tissue (5 cm long) with sinusoidal ACh profile $\mathrm{ACh}(x) = 0.6 + 0.4\cos(2\pi x/\lambda)$, where λ is the ACh wavelength. (A) Steepest APD gradient in the resulting APD profile as a function of ACh wavelength. (B) Relative error of the inverse solution (relative to the target ACh profile) as a function of ACh wavelength after 1, 10, 50, 100 and 1000 iterations. The curve after 1000 iterations is always below 1%.

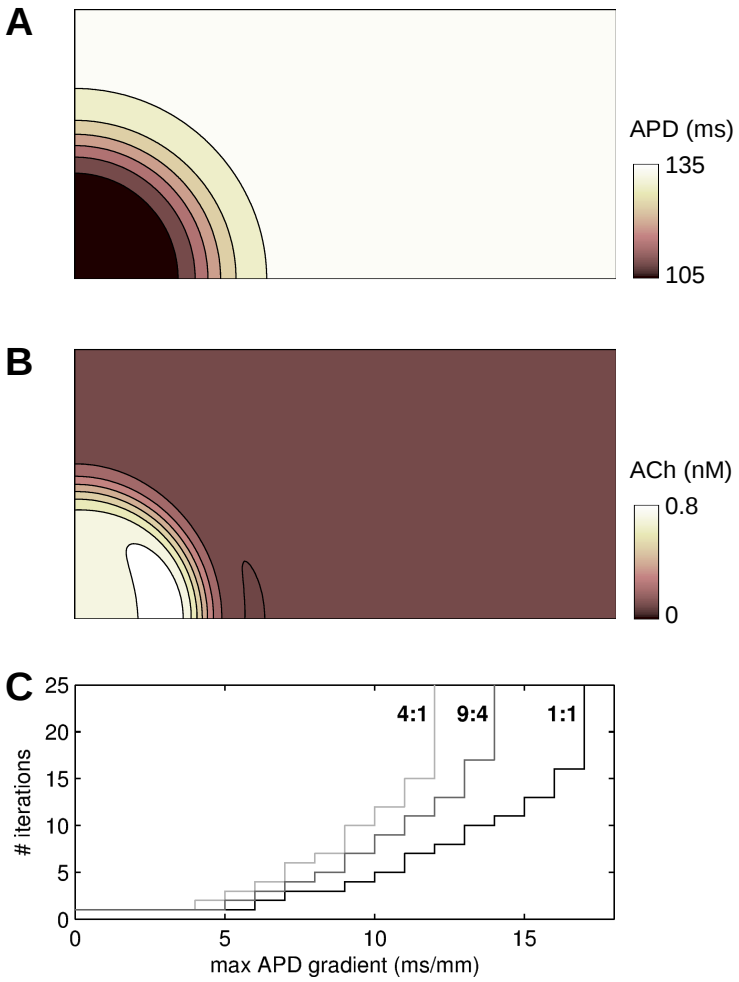

Figure 6: Solution to the inverse problem in a 5-by-2.5 cm two-dimensional tissue. The longitudinal/transverse conductivities of the tissue were 2 and 0.5 mS/cm (ratio 4:1), 1.25 and 0.67 mS/cm (ratio 9:4) and 1 mS/cm (isotropic, ratio 1:1). The longitudinal direction follows the horizontal axis. (A) Example of target APD map with a maximal APD gradient of 5 ms/mm. (B) ACh profile obtained by solving the inverse problem for the target APD map of panel A and an anisotropy ratio of 4:1. (C) Number of iterations needed to solve the inverse problem in 2D with an error < 1 ms as a function of the maximal APD gradient.

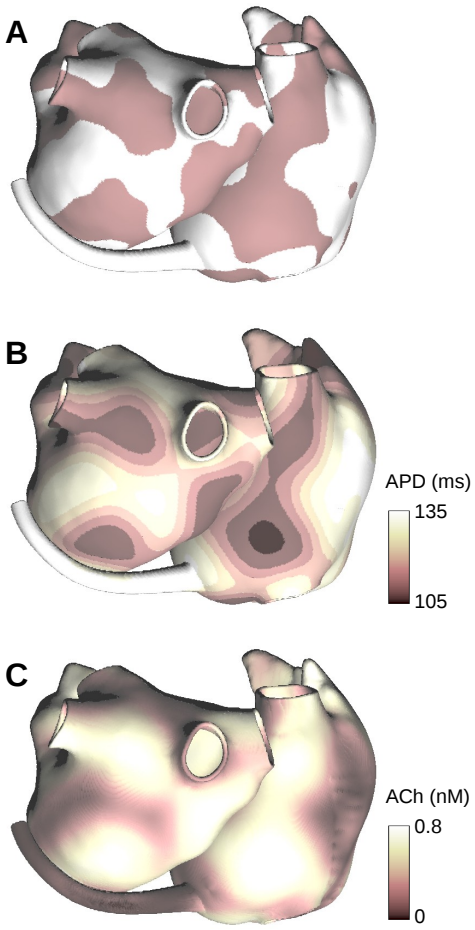

Figure 7: (A) Geometry of the atria (posterior view) with a realization of random patches of heterogeneity. (B) Generated target action potential duration (APD) map with a maximum gradient of 2 ms/mm. Contour lines are shown every 5 ms. (C) Profile of acetylcholine (ACh) concentration resulting from the solution to the inverse problem (after 15 iterations) based on the APD map of panel B.

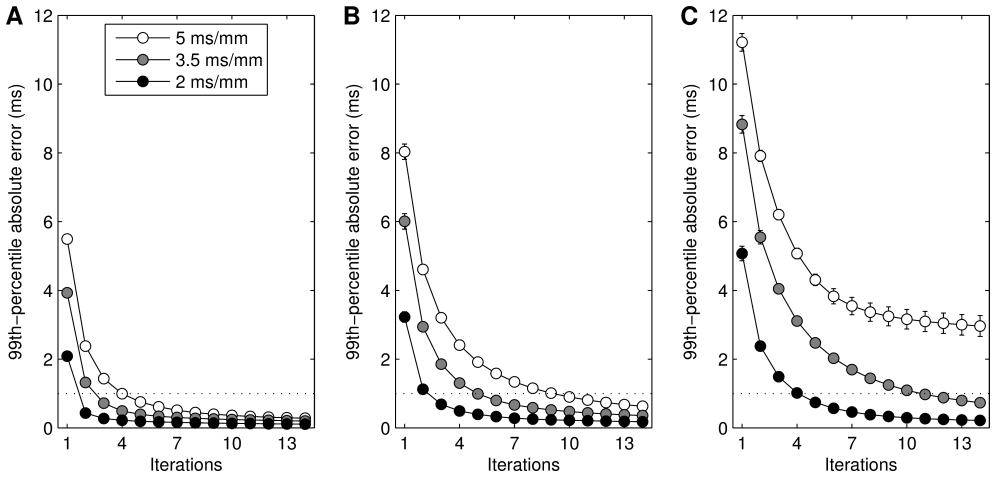

Figure 8: Convergence of the iterations in 3D assessed by the 99th percentile of the absolute error between simulated and target APD maps. Simulations were done with longitudinal/transverse conductivities of (A) 2 and 0.5 mS/cm, (B) 4 and 1 mS/cm and (C) 9 and 3 mS/cm, and APD gradients of 2, 3.5 and 5 ms/mm. Error bars represent the standard deviation over four realizations of the random patches distribution. The 1-ms threshold is indicated as a horizontal dotted line.

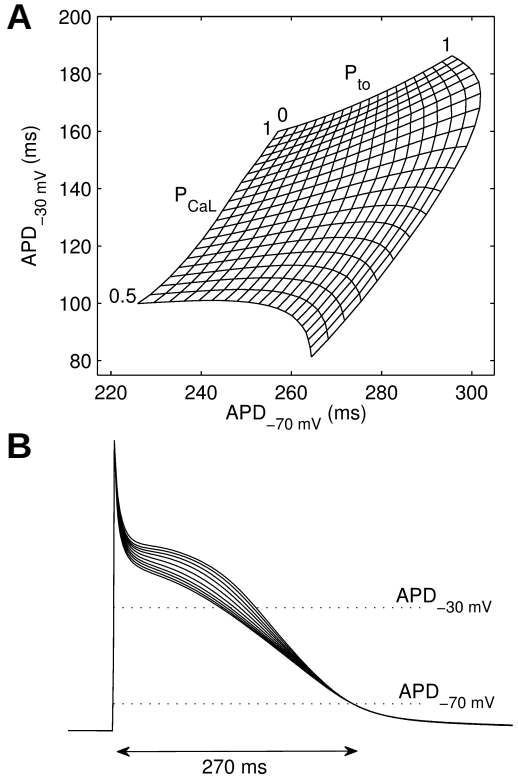

Figure 9: (A) One-to-one mapping between the parameters (P_{CaL}, P_{to}) in the range $[0.5, 1] \times [0, 1]$ and the action potential durations (APD) measures at a threshold of -70 mV and -30 mV in a single cell with Courtemanche et al. kinetics. (B) Examples of action potentials with the same APD at -70 mV but with varying APD at -30 mV.

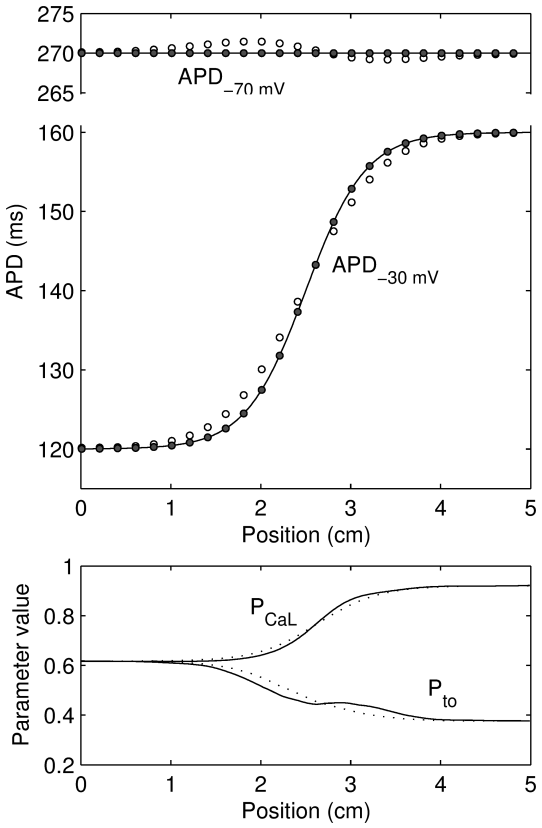

Figure 10: Two-parameter inverse problem in a 1D cable: P_{CaL} and P_{to} are simultaneously estimated based on action potential durations (APD) at -70 mV and -30 mV. *Top panel*: Target APD profiles (solid line), initial estimates (white circles) and profiles after convergence (gray circles). *Bottom panel*: Profiles of P_{CaL} and P_{to}, initial estimate (dotted lines) and after convergence (solid lines).